Journal of Electroanalytical Chemistry 950 (2023) 117880

Contents lists available at ScienceDirect

Journal of Electroanalytical Chemistry

journal homepage: www.elsevier.com/locate/jelechem

Stainless steel as an electrocatalyst for overall water splitting under alkaline and neutral conditions

Ieva Barauskienė [a,*], Giedrius Laukaitis [a], Eugenijus Valatka [b]

[a] Department of Physics, Faculty of Mathematics and Natural Sciences, Kaunas University of Technology, Studentų Str. 50, 51368 Kaunas, Lithuania
[b] Department of Physical and Inorganic Chemistry, Faculty of Chemical Technology, Kaunas University of Technology, Radvilėnų Str. 19, 50254 Kaunas, Lithuania

ARTICLE INFO

Keywords:
Oxygen evolution
Hydrogen evolution
Stainless steel
Water splitting

ABSTRACT

The development process for an effective catalyst for electrochemical water splitting must consider properties such as chemical and mechanical stability, corrosion resistance, and abundance alongside efficiency. In this work, a detailed electrochemical evaluation of four types of commercially available AISI stainless steel (302, 304, 316, and 321) was performed for their electrocatalytic activity, stability, and corrosion resistance in overall water splitting under alkaline (pH 14.00) and near-neutral conditions (pH 6.26). Using AISI plates directly as an anode or cathode, a current density of 10 mA cm^{-2} was obtained at $\eta \approx 0.38$ V for OER and $\eta \approx 0.43$ V for HER in 1 M KOH. Although all of the tested types have proved to be efficient electrocatalysts, detailed electrochemical studies have distinguished certain differences between the AISI types, depending mainly on the composition peculiarities. A detailed corrosion evaluation has revealed that although all measured stainless steels are sensitive to the oxidative environment, their corrosion rate does not exceed 3.3 μm per year.

1. Introduction

The current worldwide energy system based on fossil fuels must undergo a profound transformation to achieve the global decarbonization goals set for 2050 [1]. Low-carbon electricity from renewable sources can provide a reduction in energy-related CO_2 emissions by more than 40 % [2]. However, certain sectors requiring high-grade heat, such as industry, heavy-duty transport, etc. might find difficulties purely by means of electrification. Hydrogen has the potential to play the role of the missing link in the energy transition due to its high mass energy density [3]. Produced from renewable sources through water electrolysis, it could facilitate the revolution of the world's energy economy [4]. Electrolyzers, as devices that use electricity to split water into its constituents, offer a flexible load and can provide grid balancing services that are substantial in maximizing the employment of renewable sources [2]. Water electrolysis (WE) involves two half reactions: hydrogen evolution (HER) and oxygen evolution (OER), which both rely on the suitable electrocatalyst [5,6]. Generally, both HER and OER electrocatalysts must meet two requirements. First, electrocatalysts should demonstrate high activity with low overpotential values and provide numerous active centers. Second, both catalysts must exhibit long-term stability at high current densities without losing their efficiency [7,8]. However, nowadays environmental and economic circumstances must be taken into account when developing an electrocatalyst. Therefore, some other requirements arise, such as material abundance, its toxicity, and the impact on the environment coming from the production process, operation, and utilization or recycling. Noble metals, such as Pt, Ir and their derivatives, are attractive due to their low overpotentials, high conductivity, low Tafel slope, and long-term operation stability [9]. However, the high price and scarcity of Pt group elements in particular gave an impulse to develop an AEM (anion exchange membrane) technology that would rely on the usage of abundant and inexpensive metals or their derivatives while maintaining high efficacy of the electrolyzer [10,11]. Since the efficiency of the electrocatalyst is decided by its number of active centers and charge transfer in the bulk and on the surface, the introduction of more than one metal might help to overcome the process limitations. Various theories of intermetallic bonding, such as Brewer, Friedel, and Miedema's, suggest that phases or compounds of exceptional stability are obtained when metals with a hypo-d-electronic configuration (d^1–d^5) are alloyed with hyper-d-electronic elements (d^6–d^{19}) [12]. As a result, the level of d-orbitals of the hyper-d-electronic element increases from 3d to 5d and the exposure of d-orbitals occurs. The d-orbital is the predominant band in bonding and chemisorption [13], therefore, it determines the catalytic and electrocatalytic behavior

* Corresponding author.
E-mail address: ieva.barauskiene@ktu.lt (I. Barauskienė).

https://doi.org/10.1016/j.jelechem.2023.117880
Received 23 August 2023; Received in revised form 16 October 2023; Accepted 19 October 2023
Available online 21 October 2023

Table 1
Some properties of stainless steel by type.

Properties	Stainless steel type			
	AISI302	AISI304	AISI316	AISI321
Electrical resistivity (μΩ cm)	70–72	70–72	70–78	70–73
Density (g·cm^{-3})	7.920	7.930	7.960	7.900
Melting point (°C)	1400–1420	1400–1455	1370–1400	1400–1425

[14]. It was established that increasing the electron density directly increases the ability of metal valence electrons to participate in the formation of chemisorptive bonding [13]. As a consequence, the metal role as an electron acceptor is strengthened, while the metal role as an electron donor is weakened. Austenitic stainless steels (SS) offer a variety of metals in their composition, with the leading roles of hyper-d iron and nickel being well recognized electrocatalysts. The addition of hypo-d metals, such as chromium, molybdenum, or titanium, results in improved stability, balanced electron density, and enhanced number of active sites. Due to their high conductivity, corrosion resistance, and mechanical strength, various types of SS have been exploited in the fields of petrochemical, aviation, industrial construction, and catalysis as conductive substrates or current collectors [15,16]. Although several publications present SS as an effective, inexpensive and abundant electrocatalyst for water splitting [17], their main focus is on OER [18] by modifying the surface or removing Cr [15,16,19]. However, information on the overall water splitting that uses stainless steel is scarce. Furthermore, different authors emphasize the advantages of different types of steel and the influence of metallic additives (Mo, Ti) on the hypo-hyper-d-effect is left unexplored. As this effect has a strong influence on the electron density, the electron-donor/acceptor abilities of the metal alloy will directly affect the efficiencies of HER (donor) and OER (acceptor).

Therefore, in this work, we investigate the evolution processes of oxygen and hydrogen on different types of steels under alkaline and neutral conditions. The types selected in this work (AISI302, AISI304, AISI316, and AISI321) include some of the most common and used types that slightly differ in composition. As the composition of the AISI302 and AISI304 types contains mainly Fe, Cr, and Ni, the difference between these steels comes from the higher content of Ni in AISI304 as well as the lower carbon content. Meanwhile, AISI316 and AISI321 are enriched with Mo and Ti, respectively. Both Mo with a $4d^5 5s^1$ configuration and Ti with a $3d^2 4s^2$ configuration are considered as hypo-d elements; therefore, the introduction of them into the alloy should provide a variety of oxidation states and balance the electron density.

2. Materials and methods

2.1. Instrumental analysis

The phase structure of stainless steel was analyzed with the BRUKER AXS D8 X-ray diffractometer operating under the following parameters: wavelength $\lambda = 1.54056 \times 10^{-10}$ m for Cu-K_α radiation, Ni filter, anodic voltage 40 kV, detector position step 0.02°, and current strength 40 mA. Surface topography images were obtained using the Hitachi S-3400 N scanning electron microscope (SEM). Surface roughness was investigated with a high resolution atomic force microscope (HR-AFM) AFM Workshop (South Carolina, USA). The vibrating scanning mode (XY Resolution 0.005 nm, Z Resolution 0.003 nm, Z Linearity < 0.1 %), and the measurements were performed in Q-Box.

2.2. Electrochemical testing

Four types of standardized AISI stainless steel (AISI302, AISI304, AISI316 and AISI321) of 0.1 mm thickness were purchased from Goodfellow Cambridge Ltd. (the UK). The samples were treated with sand paper (grit 1000) and ultrasonically cleaned in an alkaline solution and acetone for 15 min. Some properties and composition of steel samples according to the standard and data obtained from the manufacturer are presented in Tables 1 and 2.

Table 2
Elemental composition of stainless steel by type.

Element (wt.%)	Stainless steel type			
	AISI302	AISI304	AISI316	AISI321
Cr	18	18	18	18
Ni	8	10	10	9
Mn	0–2			
Si	0–1	0–1	0–1	0–0.75
C	0–0.15	0–0.07	0–0.07	0–0.08
P	0–0.045	0–0.050	0–0.050	0–0.045
Ti	–	–	–	5
Mo	–	–	3	–
Fe	Balance			

Electrochemical evaluation of the activity of the samples in water splitting reactions was carried out with a potenciostat/galvanostat BioLogic SP-150 (BioLogic Science Instruments, Seyssinet-Pariset, France). A three-electrode configuration was employed, consisting of a working electrode (prepared stainless steel samples, 1 × 3 cm), a counter electrode (Pt wire, 15 cm^2), and a reference electrode (Ag,AgCl|KCl$_{(sat)}$). The experimental data were collected and treated using EC-Lab V10.39 software.

Potential-controlled electrolysis was performed in 1.0 M KOH (Chempur, Poland) and 0.1 M KNO_3 (Chempur, Poland) to construct the Tafel plots. The potential range was selected around the onset potentials of OER and HER to capture the initiation of the process. The overpotential values were calculated according to the following equation [20]:

$$\eta = E_{appl} - E_{eq} \quad (1)$$

where E_{appl} is the applied potential (V) vs Ag,AgCl|KCl$_{(sat)}$, and E_{eq} is the equilibrium potential of the OER or HER reaction at a certain pH (14.00 or 6.26).

The corrosion rate of all types of stainless steel was evaluated by potentiodynamic cycling in 1.0 M KOH and 0.1 M KNO_3 solution. The scans were performed at open circuit potential $E_{oc} \pm 200$ mV. Quantitative corrosion parameters were based on the Butler-Volmer equation [21]:

$$I = I_{corr}\left(e^{\frac{2.303(E-E_{corr})}{\beta_a}} - e^{\frac{-2.303(E-E_{corr})}{\beta_c}}\right) \quad (2)$$

where I is the measured current (A), I_{corr} is the corrosion current (A), E is the electrode potential (V), E_{corr} is the corrosion potential (V), β_a and β_c is the Tafel anodic and cathodic [21] constants (V).

The corrosion rate was calculated using EC-Lab V10.39 software according to the following equation:

$$CR = \frac{I_{corr} \bullet K \bullet EW}{d \bullet A} \quad (3)$$

where I_{corr} is the corrosion current (A), K is the constant equal to 3272 mm A^{-1} cm^{-1} year^{-1}, EW is the equivalent weight for SS (g per equivalent), d is a density (g cm^{-3}), and A is a sample area (cm^2).

Potentiostatic electrochemical impedance (PEIS) measurements were carried out in 1.0 M KOH and 0.1 M KNO_3 solutions, varying the frequency values from 10^6 to 10^{-3} Hz with a sinus amplitude of 20 mV. The iR compensation with 85 % compensation was performed at 1 Hz prior to PEIS experiments.

The obtained potentials were standardized to the reversible hydrogen electrode (RHE) by the following equation:

$$E_{RHE} = E_{Ag,AgCl} + E^0_{Ag,AgCl} + 0.059 \bullet pH$$

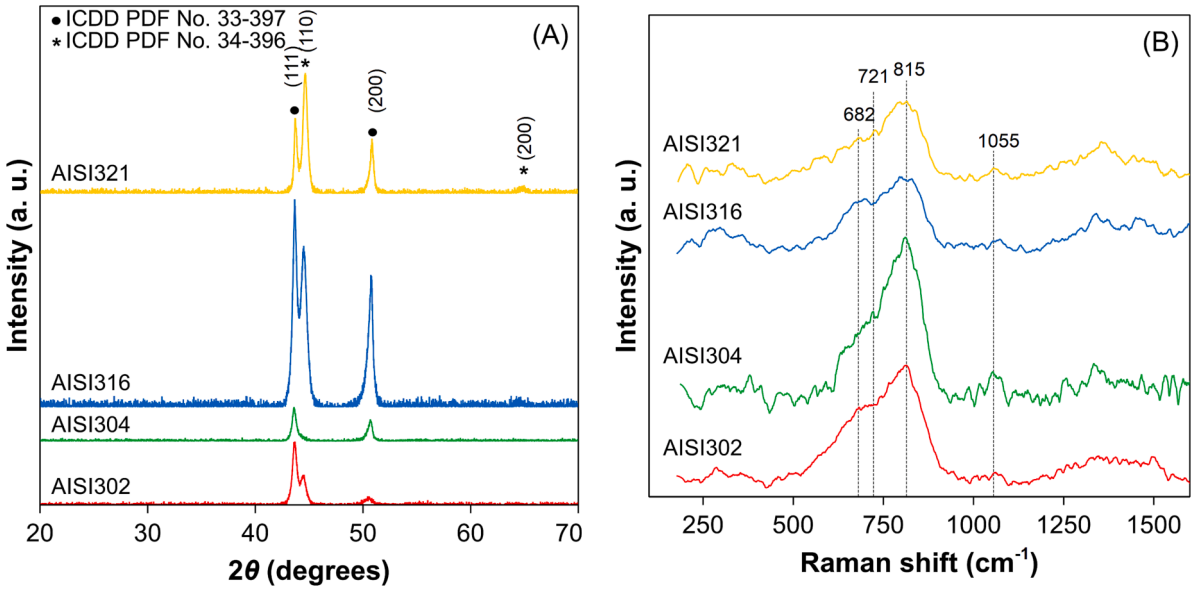

Fig. 1. XRD (A) patterns and Raman spectra (B) of stainless steel samples.

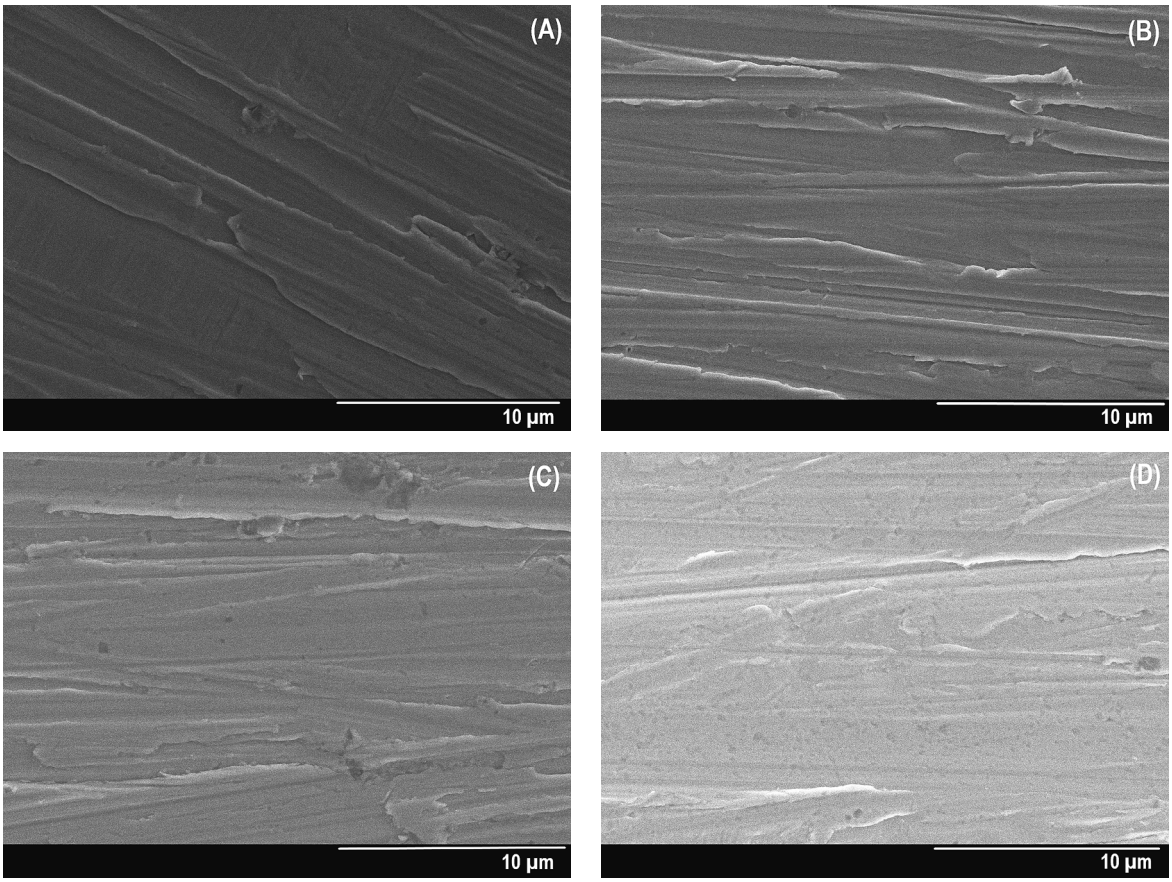

Fig. 2. Representative SEM images of stainless steels at ×5000 magnification: (A) AISI302, (B) AISI304, (C) AISI316, and (D) AISI321.

3. Results and discussion

3.1. Structural and morphological analysis

The structural characterization of stainless steel samples was performed with X-ray diffraction analysis. The data presented in Fig. 1 have revealed that only AISI304 is composed of a single cubic phase of nickel–chromium-iron with an ICDD PDF No. 33–397 (d = 2.0750, 1.7961 nm). However, the 2θ peaks at 43.646° and 50.684° related to this phase have been detected in all XRD curves. Additionally, two peaks at 44.493° and 64.625° were registered in the curves of AISI302, AISI316 and AISI321 assuming the existence of a second cubic phase in these steels. The combination of the mentioned peaks was assigned to

Table 3
Surface roughness of SS samples, where S_q is the RMS roughness and S_a is the mean roughness.

Stainless steel samples	Surface roughness							
	Before OER				After OER			
	Area size				Area size			
	33 μm × 33 μm		10 μm × 10 μm		33 μm × 33 μm		10 μm × 10 μm	
	S_q, nm	S_a, nm	S_q, nm	S_a, nm	S_q, nm	S_a, nm	S_q, nm	S_a, nm
AISI302	89.82	67.74	43.45	32.49	58.59	44.12	34.96	26.47
AISI304	91.13	76.02	68.02	57.86	85.00	62.65	55.20	43.20
AISI316	82.58	65.86	77.41	69.34	79.41	61.99	70.66	53.62
AISI321	99.88	74.48	75.64	55.02	91.12	66.68	67.78	50.09

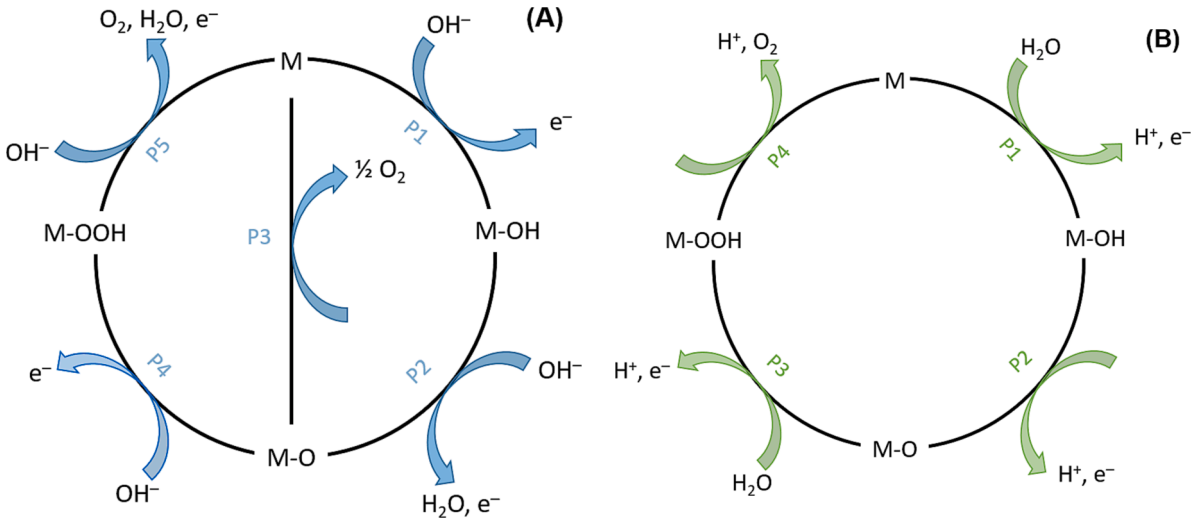

Fig. 3. The OER mechanism under alkaline [3] (A) and neutral [26] (B) conditions. The electrochemical and chemical processes that occur are indexed as P1 – P5 (P – for the process).

the alloy of iron and chromium with an ICDD PDF No. 34-396 (d = 2.0350, 1.4380 nm).

A passive film of oxide species that partly or fully covers the SS surface is rather difficult to analyze using Raman spectroscopy, since different bonds can generate the same frequencies. No significant peaks up to 500 cm^{-1} were recorded in Raman spectra of stainless steel samples (Fig. 1B), only small intensity increases. However, the spectra of AISI302 and AISI316, a slightly more noticeable increase at 289 cm^{-1} is attributed to α-Fe_2O_3 [22] Irrespective of the type of steel studied, all of them are characterized by a broad band of higher intensity with peaks at 682, 721 and 815 cm^{-1}. The signals identified in this band are associated with Fe-O vibrations in γ-Fe_2O_3, Fe_3O_4, and with Cr^{+3}-O and Cr^{+6}-O vibrations in mixed oxides [23,24]. The sharper peak around 1055 cm^{-1} and a wider band at 1250–1550 cm^{-1} usually arise due to the Fe^{+3}-O vibrations in α-FeOOH and γ-FeOOH [23] that both have orthorhombic structure only with different space groups – Pbnm and Amam, respectively [25].

The surface morphologies of AISI type steels are shown in Fig. 2. For all the samples, the surface morphology is seen to be even across the entire area with some small indentations caused by the initial surface treatment with a sandpaper. The sufficient uniformity of the surface is also confirmed by the calculation of the surface roughness (Table 3). Regardless of the type of steel, all values of RMS and mean roughness are below 100 nm. Thus, the results of SEM and AFM allow us to assume that the surface morphology is the same for all types of steel investigated in this work and does not influence the resulting differences in efficiency.

3.2. Catalytic activity in oxygen evolution

The oxygen generation process is considered to occur at the active metal sites (M) on the surface [3]. The generally assumed mechanisms of OER from both alkaline and neutral electrolytes include four electrons, as is given in Fig. 3. Specifically, under alkaline conditions (Fig. 3A), an adsorbed hydroxide ion releases the first electron to form M-OH species (P1). Then another electron and a couple of protons are released, and the active species on the surface are likely to gain the M-O form (P2). From this point on, there are two pathways for M-O transformation into O_2. Two nearby M-O species can be combined directly, producing an O_2 molecule (P3). On the other hand, the M-O complex can undergo another oxidation reaction after adsorption of the OH^- ion, resulting in the formation of M-OOH (P4). Finally, it participates in proton-coupled oxidation that releases O_2 and H_2O molecules (P5). Meanwhile, under neutral conditions (Fig. 3B) the mechanism is based on the decomposition of water molecules adsorbed on the catalyst surface. Yet, the intermediates formed, including OH*, O* and OOH*, remain the same regardless of whether they are in neutral or alkaline media [26]. Concerning the difficulty of the OER mechanism, the catalyst surface plays an extremely relevant role in providing sufficient concentration of active sites as well as ensuring optimal binding energy of OER intermediates. It was determined [27] that strong oxygen binding can hinder the formation of M-OOH species; meanwhile, too weak binding can result in sluggish M-O formation. It is known [28] that right after the immersion in the alkaline solution, the surface of stainless steel is covered with OH^- ions that from a monolayer of M-O, M-OH, or M-OOH. Therefore, the exact mechanism of OER might have some deviations from the theoretical one in Fig. 3.

Table 4
Oxygen evolution parameters of stainless steel samples.

Parameters	Stainless steel type			
	AISI302	AISI304	AISI316	AISI321
Alkaline media				
Onset OER potential (mV)	1572	1574	1570	1573
Overpotential at onset (mV)	342	344	340	343
Tafel slope b (mV dec^{-1})	35 59	35 73	31 81	39 96
Overpotential (mV) at 10 mA cm^{-2}	381	389	381	389
Retention after 24 h OER (%)	97.5	94.7	95.5	95.3
Neutral media				
Onset OER potential (mV)	2073	2097	2066	2079
Overpotential at onset (mV)	843	867	836	849
Tafel slope b (mV dec^{-1})	180	154	185	173
Overpotential (mV) at 10 mA cm^{-2}	1242	1386	1246	1278
Retention after 24 h OER (%)	99.3	96.6	98.4	98.5

The catalytic evaluation of the prepared stainless steel samples began with the examination of its ability to promote oxygen formation. Steady-state linear sweep voltammograms (LSV) were recorded in 1.0 M KOH and are displayed in Figs. S1 and 4, while quantitative parameters are given in Table 4. When the anodic potential was scanned beyond 1.5 V, a rapid increase in current values was observed, accompanied by intensive formation of O_2 on the stainless steel surface. No catalytic current was observed earlier than 1.5 V (Fig. 4A). Regarding the relation between the stainless steel type and its activity in OER catalysis, the LSV curves present a visual difference in their behavior. The onset potential of oxygen formation overlaps between various types of SS and the difference in E_{onset} values is within the limits of error (Table 4). As a result, overpotential values between different steels vary by no more than 5 mV from 340 from AISI316 to 345 mV for AISI304. However, a further increase in potential values affects the current density differently. AISI316 has been found to provide the highest current values among other types tested in this work. It also required a smaller overpotential value to reach the current density of 10 mA cm^{-2} (381 mV) or 100 mA cm^{-2} (680 mV). This advantageous activity could be attributed to the presence of molybdenum in the composition of AISI316. According to Zhang

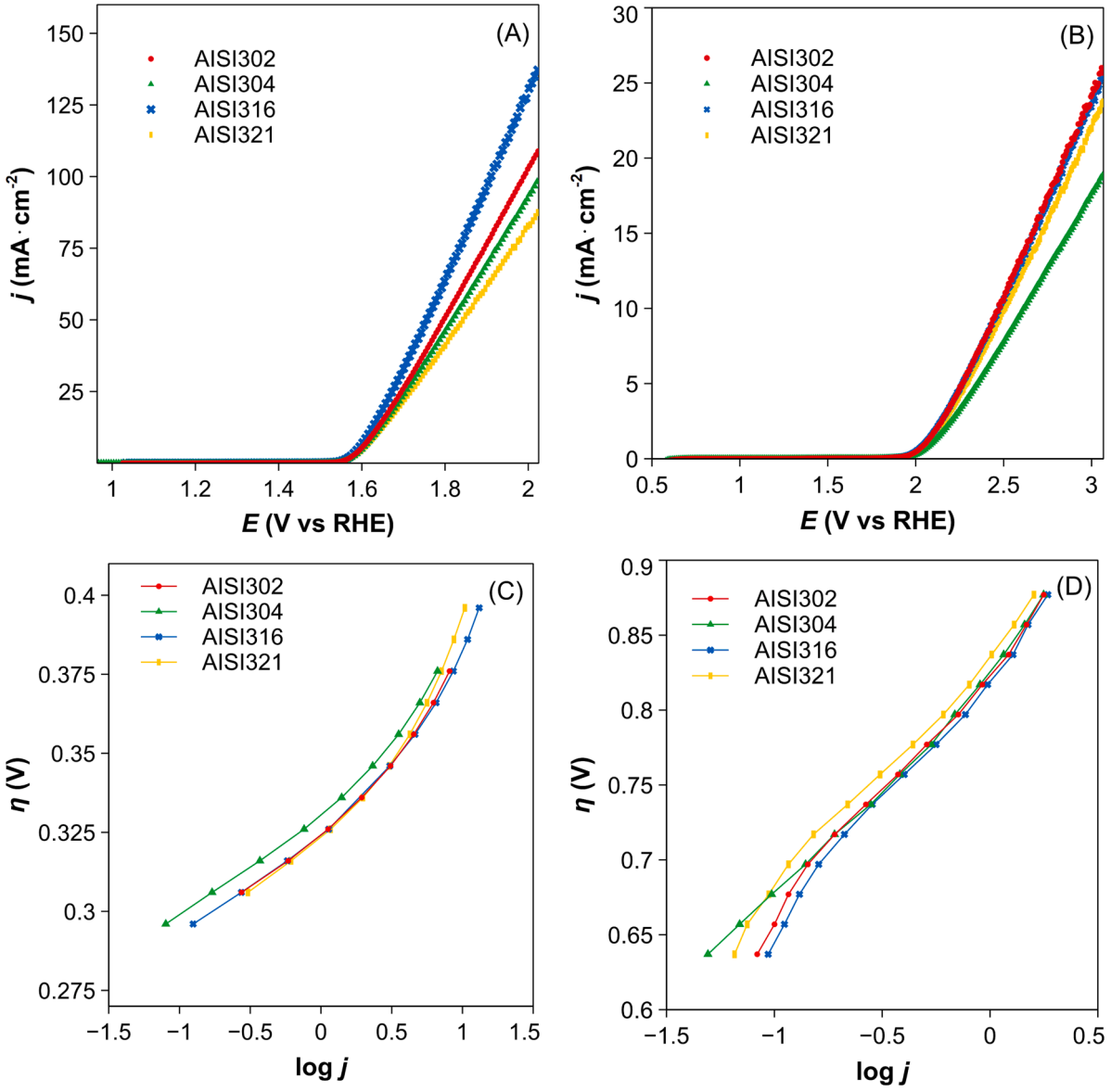

Fig. 4. Linear sweep voltammograms of stainless steels in 1.0 M KOH (A) and 0.1 M KNO_3 (B) at a scan rate of 20 mV s^{-1}. Tafel plots of stainless steel samples in 1.0 M KOH (C) and 0.1 M KNO_3 (D).

et al. [29], Mo has a strong electron-deficient structure that leads to the large extent d-electron delocalization and electron transfer. Therefore, the alloy is more likely to act as an electron acceptor promoting precisely the oxidation of water [13,30]. Furthermore, the enhanced hydrophilic properties of Mo facilitate the adsorption of water molecules and hydroxo- species [29,31]. Although AISI302 does not possess any additives that increase activity in its composition, it is only slightly inferior to the AISI316 type.

The quantitative parameters of the OER, such as the onset potential, the overpotential at the onset and 10 mA cm^{-2}, are rather similar for both AISI316 and AISI302 at lower potentials. However, it appears that the surface of AISI302 cannot generate oxygen at the same rate as that of AISI316 at higher overpotentials as it reaches 100 mA cm^{-2} at 760 mV. When comparing the types of AISI302 and AISI304 which differ only in nickel content, it can be seen that AISI302 steel is more active despite the lower Ni content. That may also be attributed to the electronic density which depends both on the electronic configuration of the catalyst lattice and the prevailing configuration on the catalyst surface [32]. XRD analysis revealed that AISI302 is a two-phase alloy in which the hyper-d-element Fe and the hypo-d-element Cr constitute a separate phase. The existence of such a synergy might boost the surface abilities of bonding and chemisorption of intermediates. AISI321 steel appears to be the least favorable for oxygen evolution. Although its overpotential reaches the same value as AISI304 at 10 mA cm^{-2} (389 mV), the further generation of oxygen on its surface occurs more sluggishly. This may be related to a more passive surface, insufficient amounts of active centers, and poorer charge transfer. Although AISI302 and especially AISI321 have not been extensively investigated as catalysts, OER studies conducted with unmodified AISI304 and AISI316 steels under alkaline conditions have generated results similar to those obtained in this work [15,19].

Long-term electrolysis (Fig. S3) has revealed the behavior of stainless steels throughout constant O_2 generation for 24 h. All samples examined were able to maintain a stable potential value at 10 mA cm^{-2} since their retention exceeded 94 %. As expected, AISI302 and AISI316 types have demonstrated their superiority as the first was able to maintain 97.5 % and the slowest potential loss, while the second has upheld the determined current density at the lowest overpotential.

Since most of the research on the electrocatalytic properties of stainless steels in the OER focuses on testing in an alkaline medium, there is a lack of information on the behavior of steels under neutral conditions. Basic electrolytes are preferred for the OER process rather than HER, which usually requires adsorbed protons to overcome the reduction to the H_2 molecule and works better in acidic media [33]. The demand for simultaneous generation of O_2 and H_2 encourages research of this process under neutral or near-neutral conditions. The reduction of the pH values to near-neutral by replacing the electrolyte of potassium hydroxide with potassium nitrate decreases the concentration of hydroxide ions and the activity as well. Furthermore, a near-neutral environment is favorable for protons to be generated by the surface reactions [34] as it supports HER.

Fig. 4B displays the OER activity of stainless steels in 0.1 M KNO3, which holds a pH value of 6.26. It can be noticed that the pattern of catalytic behavior between different types of steel is similar as the nature of the curves overlaps. However, the onset potential determined by the tangent method highlights some differences between steel types (Table 4) as the OER on AISI316 starts at 2.06 V, while it requires 2.09 V to begin on AISI304. This result suggests that a two-phase structure could be an advantage in providing a variety of oxidation states for water adsorption and decomposition, as all three two-phase steels (302, 316 and 321) have required smaller overpotentials at 10 mA cm^{-2} (1.24–1.27 V) than a single-phase AISI304 (1.38 V). The absence of a clear difference between the types AISI302, AISI316 and AISI321 might be associated with the electrode surface, which sets its equilibrium after immersion into the solution. Open circuit potential (OCP) measurements have shown that all types of AISI gain slightly negative OCP values (0.7 V ± 0.08 V) in 1.0 M KOH solution. The metal surface then is favorable to go through oxidation and corrosion, which leads to the formation of oxide, hydroxide, or oxyhydroxide species on the surface. Meanwhile OCP values of AISI plates in 0.1 M KNO_3 solution reached their equilibrium at slightly positive values (0.79 V ± 0.04 V). This result signifies that metals in the SS composition tend to maintain their metallic form on the surface.

The Tafel equation is a common tool that is used to determine the kinetics of the electrochemical reaction [20]:

$$\eta = a + b\log j \tag{4}$$

where, η is the overpotential, a and b are Tafel constants and j is the current density. The lower value of the Tafel slope (or constant b) signifies greater charge transfer. The Tafel slope value also defines the rate-determining step (RDS) of the catalysis process. The lower value of b usually means that the RDS is at the end of the overall process. In this work, Tafel plots were constructed not from LSV results but rather from potential-controlled electrolysis (Fig. S2). Experimentally obtained results that are shown in Fig. 4B and D correlate greatly with LSV regularities. Due to the presence of Mo in AISI316 it exhibits better charge transfer properties and results in the lowest Tafel constant value regarding OER in alkaline electrolyte (31 mV dec^{-1}). The constant b values of AISI302 and AISI304 only match at the beginning of the process generating a value of 35 mV dec^{-1}. Later, when OER progresses, AISI302 exhibits lower overpotentials (59 vs 73 mV dec^{-1}). This might happen because of the differences in binding strength of the OER intermediates on the surface. If the surface overbinds the OER derivatives, the process itself will become more sluggish and energy consumptive. Meanwhile, under neutral conditions, AISI304 steel exhibited the lowest coefficient b, which differed from other types by 20–30 mV. Although the difference is not significant, it shows that although oxygen generation on the surface of this steel starts a bit slower, then presumably the limiting processes move further up the chain of the mechanism (Fig. 3B).

When evaluating Tafel constants, Antipin and Risch [21] have interpreted the b values by performing calculations according to the different surface coverage θ_k:

for the forward reaction: $j = n \bullet F \bullet k^0_{+i} \bullet e^{(1-\beta)\bullet f\bullet\eta_i} \bullet a_i \bullet \theta_k$, (5)

for the backward reaction: $j = n \bullet F \bullet k^0_{-i} \bullet e^{-\beta\bullet f\bullet\eta_i} \bullet a_i \bullet \theta_k$, (6)

where n is the number of electrons involved, F is the Faradaic constant, $k^0_{\pm i}$ is the kinetic constant, β is the symmetry coefficient set equal to 0.5, $f = \frac{RT}{F}$, η_i is the overpotential of the i^{th} step, and a_i is the activity of involved species.

The authors [21] have selected presumable values of the activity of the involved species (OH, H_2O or dissolved O_2) as $a_{OH} = 1$ corresponding to the pH = 14.00, $a_{H_2O} = 1$, and $a_{O_2} = 0.001$. Taking into account the case of intermediate binding strength of the OER species, two Tafel slopes were obtained, respectively, 24 and 118 mV dec^{-1} depending on the surface coverage. b = 24 mV dec^{-1} was determined when θ_k of M was dominant, while when the surface was covered with M−OH and M−O ($\theta_k \approx 0.06$) the value of b increased to 118 mV dec^{-1}. Anyway, when the surface coverage is not constant, the Tafel slope acquires intermediate values depending on the overpotential or current density.

Another relevant parameter affecting the Tafel constant is the anodic transfer coefficient, α_a, which is defined as a part of the electrostatic potential energy that determines the oxidation rate [35]. Although α_a can be easily calculated for a reaction when a single electron is transferred, its reliability becomes questionable for complex electron reactions such as oxygen evolution. Therefore, the symmetry coefficient β instead of α is often used to describe the RDS, as it is found to be significantly slower than other steps. For multistep reactions, the relation between b and β is expressed as follows [36]:

$$b = \left(\frac{\partial E}{\partial \log i}\right)_{pH} = \frac{2.303RT}{F} \bullet \frac{1}{n_b + \beta n_d} \tag{7}$$

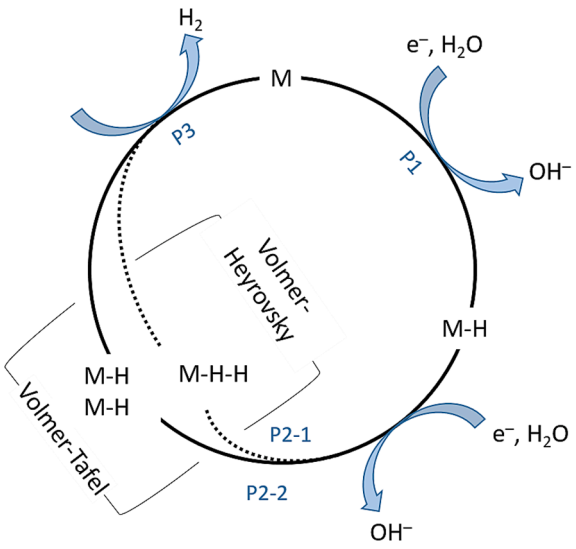

Fig. 5. The HER mechanism under alkaline/neutral conditions.

where, n_b is the number of electrons transferred before the RDS and n_d is the number of electrons transferred during the RDS (Table S1).

According to the simulations with the symmetry coefficient in Fig. S4, it can be seen that the values of the Tafel slope decrease drastically with more electrons transferred before the RDS. Although theoretical calculations may not match actual results due to noise, side reactions, or other factors, they provide information on the dominant RDS at different overpotentials. It has been observed that the P2 step (Fig. 3) dominates in the case of small overpotentials in the alkaline medium. Meanwhile, after intensifying the reaction in the range of higher overpotentials due to the formation of gas bubbles, which probably cover part of the surface, the charge transfer is hindered and the rate of the overall reaction starts to depend on the rate of the P1 step (Fig. 3). Meanwhile, in neutral solution, the generation of oxygen from water molecules rather than hydroxide ions appears to be much slower and requires energy, as the *P*1 step is the RDS throughout the overpotential range investigated in this work. The Tafel slopes, calculated in this work, suggest that the symmetry coefficient should be in the range of 0.5–0.9 in an alkaline electrolyte and 0.3–0.4 in a neutral electrolyte. It can be assumed that oxygen generation from water molecules rather than hydroxide ions is much less effective since only 30–40 % of potential energy is used to obtain the final product.

XRD (Fig. S7A) and Raman (Fig. S7B) analysis performed after 24 h oxygen evolution on stainless steel samples in 1.0 M KOH solution has not disclosed any significant changes in stainless steel surfaces. However, from the Raman spectra it can be expected that oxides, especially α-Fe_2O_3 and γ-Fe_2O_3, instead of oxyhydroxides began to dominate the surface after intensive O_2 generation, as intensities in the area of values greater than 1000 cm^{-1} decreased slightly. Surface morphology studies by SEM analysis (Fig. S8) also did not record significant surface changes or signs of deterioration. Surface roughness measurements (Table 3) revealed a slight decrease in roughness, which is probably related to the replacement of oxyhydroxide species with oxides. However, the roughness results do not exceed 100 nm, so long-term operation can be expected to not significantly affect the mechanical stability of the catalyst.

3.3. Catalytic properties in hydrogen evolution

Hydrogen evolution under either alkaline or neutral conditions begins with the adsorption of a water molecule onto the catalyst surface (Fig. 5). Adsorbed H_2O undergoes dissociation and reduction to release OH^- ion while the proton stays bound to the metal surface (Volmer step, P1). Then, there are two pathways for further M−H transformation. The Heyrovsky step includes the reduction of another water molecule that forms an M—H—H intermediate (P2-1) which is released from the surface as a H_2 molecule (P3). Meanwhile, a process described as the Tafel step (P2-2) involves two close H atoms that combine directly into the H_2 molecule (P3) [7,37].

The evaluation of the catalytic ability of coatings to promote HER began with steady-state linear sweep voltammograms (LSV) recorded in 1.0 M KOH and 0.1 M KNO_3 at a scan rate of 20 mV s^{-1}. Although alkaline conditions are not favorable for HER, all of the stainless steels were able to efficiently catalyze this process (Fig. 6A). Once again, AISI316 has demonstrated its superiority over other types with its lower onset potential (–0.332 V) and overpotential at E_{onset} as well (332 mV) that are ≈20 mV lower than others (Table 5). As in the case of OER, this advantageous behavior might be attributed to the Mo additive. Mo-containing alloys, especially those with Ni, offer enhanced ability to reduce the energy barrier of water dissociation [31]. Therefore, the presence of Mo-Ni might accelerate the hindered kinetics of the Volmer step (P1) of HER under alkaline conditions. Meanwhile, the differences in activity among the other types are insignificant, and the curves resemble each other. The similarity between AISI302, AISI304, and AISI316 is also confirmed by the onset and overpotential in Table 5 where their values differ by no more than 10 mV.

Compared to the Pt catalyst, which binds adsorbed hydrogen thermoneutrally at $\Delta G_H \sim 0$ eV, Fe, Ni, and Mo tend to overbind intermediates regarding their position on the left branch of volcano plot of the exchange current density vs. hydrogen binding energy [38,39]. The Sabatier principle says that too strong binding leads to difficulties in removing reaction products from the surface; meanwhile, too weak binding results in poor adsorption of the reactants [38,40]. However, the mentioned plots reflect only the potential catalytic activity of individual metals. The introduction of other metals to form alloys can modify the electronic structure and hydrogen adsorption energy as well [31]. It should also be noted that the metal surface undergoes the oxidation reaction in an aqueous environment resulting in the formation of various oxide species on the surface [28]. These processes inevitably affect the electronic properties of the catalyst surface which are responsible for the optimal adsorption of reactants and desorption of products.

Unlike OER, the sample of AISI321 has exhibited a higher initial activity in HER with the overpotential of 349 mV dec^{-1} at E_{onset} comparable to the AISI302 and AISI304 types. DFT calculations conducted by Lu et al [39], described the addition of Ti to the Cu catalyst, since both Ti and Cu tend to bind HER intermediates too strong and too weak, respectively. Theoretical simulation suggested 5 % Ti to demonstrate the best results, as lower Ti amount would not have guaranteed a sufficient number of active sites; meanwhile, a higher amount would have created inactive sites. Moreover, this result, along with OER activity in neutral media (Fig. 4B), suggests that the 5 % Ti additive creates a surface more favorable for the adsorption of water molecules rather than OH^- ions.

Comparing the dynamics of HER in an alkaline and neutral environment, Fig. 5 clearly identifies that the neutral pH supports this reaction as it begins at a lower overpotential value (Fig. 6B) though both reaction mechanisms involve H_2O molecules. The experimental results obtained from linear sweep of all samples in 0.1 M KNO_3 did not identify any type of steel as the most effective. On the contrary, all steels have demonstrated almost analogous catalytic activity. Only the AISI302 type has generated a slightly higher current density at the higher cathodic potentials (20–30 mV lower overpotential at 10 mA cm^{-2}) (Table 5), but the nature of the curve at the beginning of the HER is the same as for other types. Taking into account the cathodic region, the reduction of nitrate ions to nitrite ions inevitably takes place at potential values from −0.5 V to −1.0 V in the potassium nitrate electrolyte [41]:

$$NO_3^- + H_2O + 2e^- \rightarrow NO_2^- + 2OH^-$$

This reaction causes an increase in pH at the electrode/electrolyte interface by the generation of hydroxyl ions, hindering the hydrogen

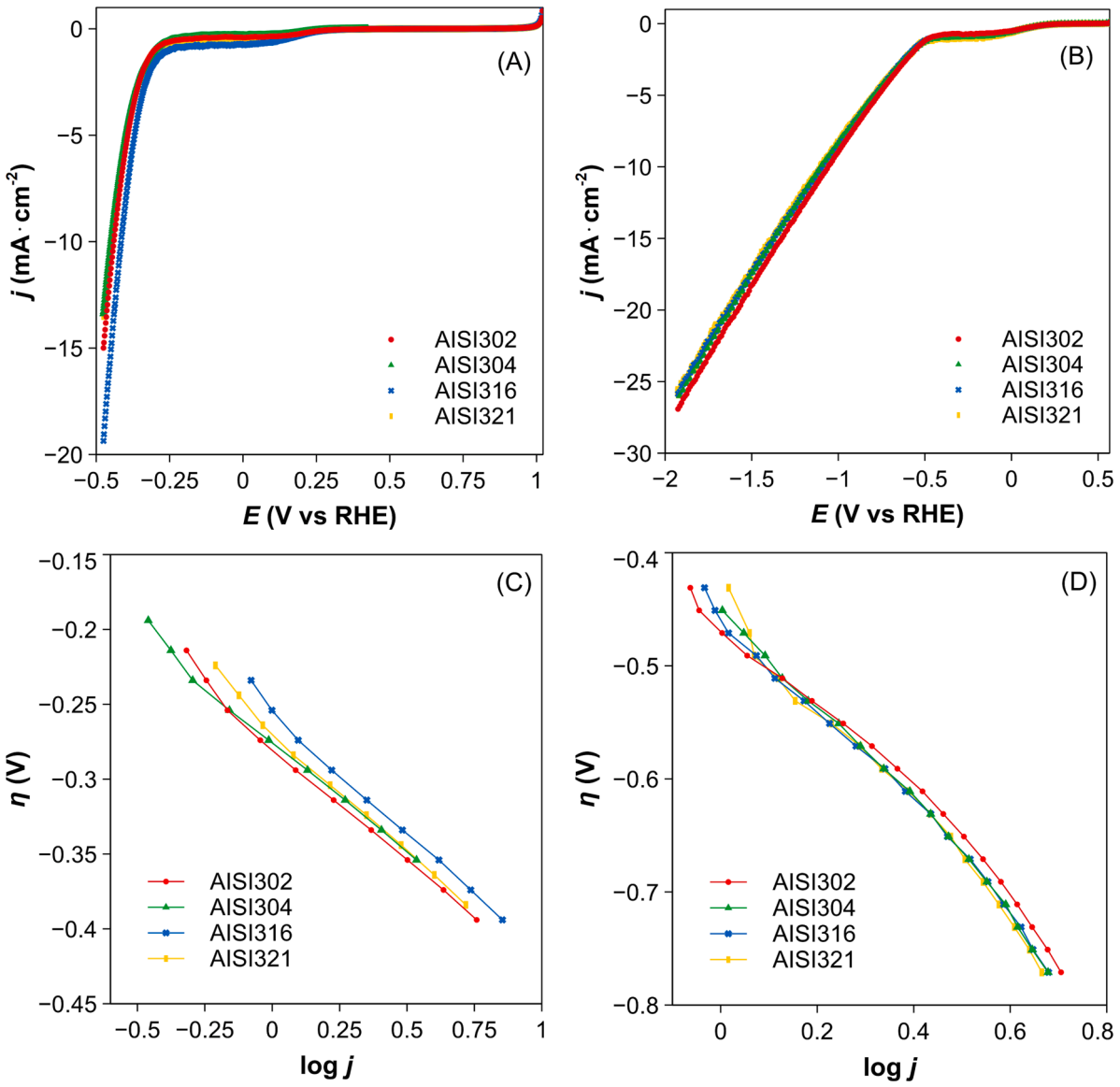

Fig. 6. Linear sweep voltammograms of stainless steels in 1.0 M KOH (A) and 0.1 M KNO_3 (B) at a scan rate of 20 mV s^{-1}. Tafel plots of stainless steel samples in 1.0 M KOH (C) and 0.1 M KNO_3 (D).

evolution and presumably shifting its onset potential further toward the cathodic side. An attempt was made to reduce this side process by intensive mixing of the electrolyte.

Investigation of HER kinetics by applying the Tafel equation (4) has revealed the complexity of the reaction itself, as all Tafel constants obtained in this work were greater than 120 mV dec^{-1} (Table 5). It is generally accepted that the Tafel slopes for the Volmer (Fig. 5, P1), Heyrovsky (P2-1), and Tafel (P2-2) stages are equal to 120, 40 and 30 mV dec^{-1}, respectively. However, it should be noted that these values depend significantly on the concentration of HER intermediates on the surface of the electrocatalyst (surface coverage θ). Theoretical calculations show that the Heyrovsky process, as an RDS, can reach values of 120 mV dec^{-1} when $\theta_H > 0.6$ [42]. This means that the value of b of 120 mV dec^{-1} cannot always be directly related to the Volmer stage. Furthermore, the theoretical values of the Tafel constants of 30, 40 and 120 mV dec^{-1} are not obtained at low overpotentials, then the interpretation of the results is related to large errors, at the same time incorrect determination of the rate limiting step.

By applying the same method of simulation of the Tafel slopes to the HER, numerical values of the constant at different values of the symmetry coefficient were obtained (Table S1 and Fig. S4). As in the OER, this model suggested that the rate of hydrogen evolution is also determined by the first step of the overall mechanism (Fig. 5). This may be related to the hindered kinetics of hydrogen evolution from the alkaline electrolyte, because an important product of the Volmer reaction in an alkaline medium is the hydroxide anion, which increases the local pH value, and thus complicates the process of water dissociation. In the alkaline electrolyte, where only hydrogen evolution occurs, the obtained values of the b constant suggest that the symmetry coefficient β should vary between 0.2 and 0.4. Meanwhile, the Tafel slopes in the neutral electrolyte are found to be above the simulated values presumably due to the competition between HER and nitrate reduction.

3.4. Evaluation of corrosion

Metallic iron, which constitutes the largest part of stainless steel, forms a natural oxide layer of (oxy)hydroxide when exposed to air or under aqueous conditions [43]. Although Cr, Ni, and Mn are designed to prevent iron from oxidation, corrosion under either alkaline or neutral conditions is inevitable. Lyons and Brandon [44] suggested, that FeO_4^{2-}

Table 5
Hydrogen evolution parameters of stainless steel samples.

Parameters	Stainless steel type			
	AISI302	AISI304	AISI316	AISI321
Alkaline media				
Onset HER potential (mV)	−353	−355	−332	−349
Overpotential at onset (mV)	353	355	332	349
Tafel slope b (mV dec^{-1})	263 151	248 143	229 158	228 159
Overpotential (mV) at 10 mA cm^{-2}	−438	−432	−424	−442
Retention after 24 h HER (%)	94.6	99.5	98.9	99.9
Neutral media				
Onset HER potential (mV)	−551	−566	−518	−564
Overpotential at onset (mV)	551	566	518	564
Tafel slope b (mV dec^{-1})	409	465	439	473
Overpotential (mV) at 10 mA cm^{-2}	−1059	−1101	−1091	−1108
Retention after 24 h HER (%)	97.0	99.5	96.8	98.1

ions are the active species in alkaline OER, although Fe^{6+} species were not directly detected on the iron surface during oxygen evolution. Therefore, it could be that some intermediate derivative of Fe_2O_3, Fe_3O_4 or FeOOH is the active center of the iron surface. According to the corrosion mechanism proposed in 1981, migration between oxygen anion vacancies at the Fe-film interface and Fe cation vacancies is the cause of oxide layer formation. However, since the exact structure and composition of the stainless steel catalyst after immersion in aqueous electrolyte are unknown, the surface should be treated as a mixture of metallic Fe and various oxide species.

Metallic nickel also forms some form of oxide in the presence of alkaline solution [45]. The variety of oxide species (NiO, NiOOH, Ni$(OH)_2$) should be taken into account when discussing the OER activity of stainless steel, since they are considered as the possible real active centers of metallic Ni [43]. Louie and Bell [46] have determined that the incorporation of Fe in the structure of NiOOH decreases the oxidation state of Ni from ~3.2 to ~2.5. Anantharaj et al. [47] emphasized the advantageous impact of Fe presence in NiOOH since the common structure $Ni_xFe_{1-x}OOH$ acts great as the active centers in OER. Therefore, as metal oxide derivatives are likely to be the active centers in oxygen evolution, the metallic nature of the bulk catalyst ensures a great conductivity and mechanical and chemical stability of stainless steels. These benefits are usually the properties that oxide catalysts lack.

The corrosion parameters of the four types of stainless steel were determined in solutions of 1.0 M KOH and 0.1 M KNO_3. Corrosion was investigated using potentiodynamic polarization around the open circuit potential (OCP) values. After the constant OCP values were reached, the samples were cathodically and anodically polarized in the potential range of OCP ± 200 mV. The CV curves (Fig. S5) of the samples did not exhibit any redox peaks, either in alkaline or neutral solutions. However, the curves differ in shape since the alkaline medium generates small-area voltammograms with nearly equal forward and reverse parts of the curves. Meanwhile, CVs in KNO_3 that produce a larger area may be attributed to double-layer capacitance processes. There is also a noticeable difference between the positive (anodic) and negative (cathodic) electric charge consumed during these scans (Fig. S6). Although anodic corrosion is a fairly well-studied process, there is little information on the cathodic reactions that occur on the steel surface. It is most likely that during cathodic corrosion, the oxygen dissolved in the electrolyte diffuses toward the electrode surface and then the reduction reaction takes place [48]. As a result, hydroxyl ions are formed, increasing the local pH:

$$O_2 + 4e^- + 2H_2O \rightarrow 4OH^-$$

In particular, AISI302 type steel is distinguished by the consumption of the cathodic charge, especially in the KOH solution. However, in accordance with the consumption of anodic charge, the oxidation processes on its surface are certainly not the most intense. It appears that the surface of AISI302 is more favorable for the supply of electrons, presumably due to the weakest d-effect and the two-phase structure.

The corrosion results in the form of a Tafel plot are displayed in Fig. 7 where the intersection between the cathodic and anodic slopes indicates the corrosion potential (E_{corr}) and the current density (j_{corr}). Regardless of the pH value of the electrolyte, the tendency of AISI302 and AISI316 to oxidize is clearly visible, as their E_{corr} values shift more toward the cathodic side (658 and 695 mV in 1.0 M KOH, respectively). This means that under conditions where there is no electrical current flowing through the system, anodic processes will dominate the steel surface. The values of j_{corr} for different types are more scattered within the range of microamperes. During this experiment, AISI302 was found to

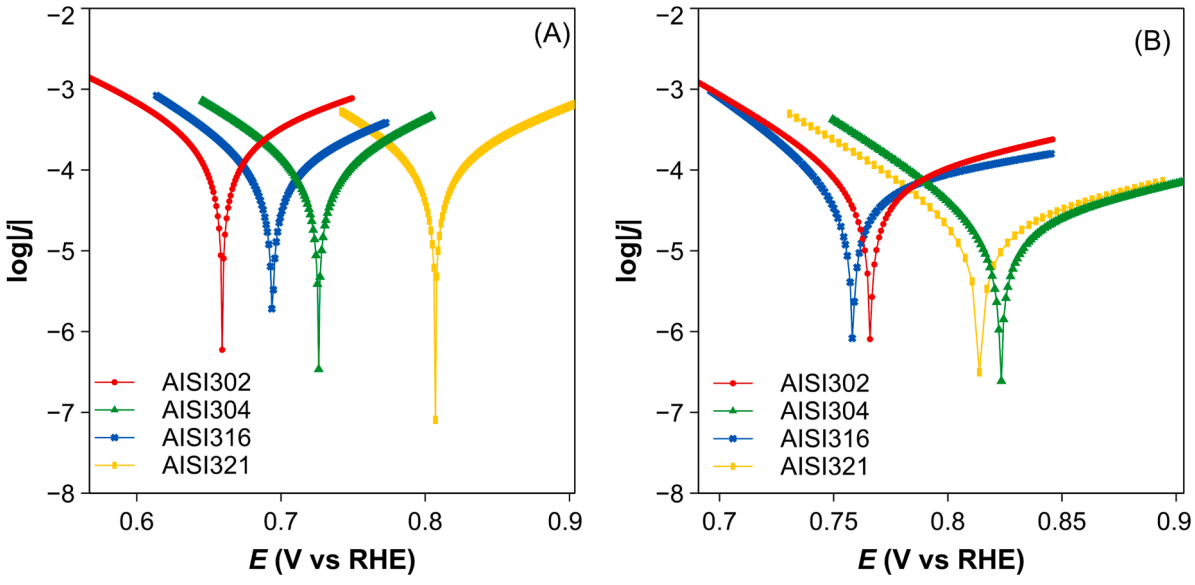

Fig. 7. Tafel fits to the corrosion measurements of stainless steel samples in electrolytes of 1.0 M KOH (A) and 0.1 M KNO_3 (B).

Table 6
Corrosion parameters for different types of stainless steel.

Parameters	Stainless steel type			
	AISI302	AISI304	AISI316	AISI321
Alkaline media				
E_{corr} (mV)	658	727	695	807
j_{corr} (μA cm^{-2})	0.286	0.117	0.123	0.158
β_a (mV)	194.2	127.3	152.0	153.1
β_c (mV)	128.8	100.4	94.6	114.4
Corrosion rate (μm per year)	3.27	1.34	1.43	1.80
Neutral media				
E_{corr} (mV)	766	823	758	814
j_{corr} (μA cm^{-2})	0.080	0.022	0.063	0.023
β_a (mV)	164.7	155.3	215.8	156.0
β_c (mV)	63.3	57.2	52.2	62.0
Corrosion rate (μm per year)	0.92	0.25	0.73	0.26

generate an almost twice higher value of corrosion current in an alkaline solution than other types. However, as determined in Fig. S6, the general current of the corrosion process in 1.0 M KOH is increased precisely by the cathodic processes taking place on the surface of AISI302. Meanwhile, as expected, the corrosion processes under neutral conditions are much slower since the oxidizing environment is not so harsh in 0.1 M KNO_3. The j_{corr} values decrease from 1.9 (for AISI316) to 6.9 (for AISI321) times after changing the solution (Table 6). Summarizing the corrosion current and rate values, it can be said that the AISI302 type has the highest corrosion tendency, while the AISI304 type appears to be the most corrosion resistant, presumably due to the single phase structure. The parameters that inform about the kinetics of both anodic and cathodic corrosion, Tafel slopes β_a and β_c – should be taken into account. In general, the Tafel constant provides additional information on the reaction rate and limiting stages. The calculation of these parameters has revealed a somewhat different regularity. Although AISI302 steel has generated the highest current density and corrosion rate, it is likely that it will not accelerate significantly at higher cathodic or anodic potentials, as its values of β_a and β_c have demonstrated the highest overpotential per decade of current density under both alkaline and neutral conditions.

PEIS measurements at the onset potentials of the OER and HER were conducted to investigate the charge-transfer processes at the electrode/electrolyte surface and throughout the solution. Fig. 8 shows the Nyquist

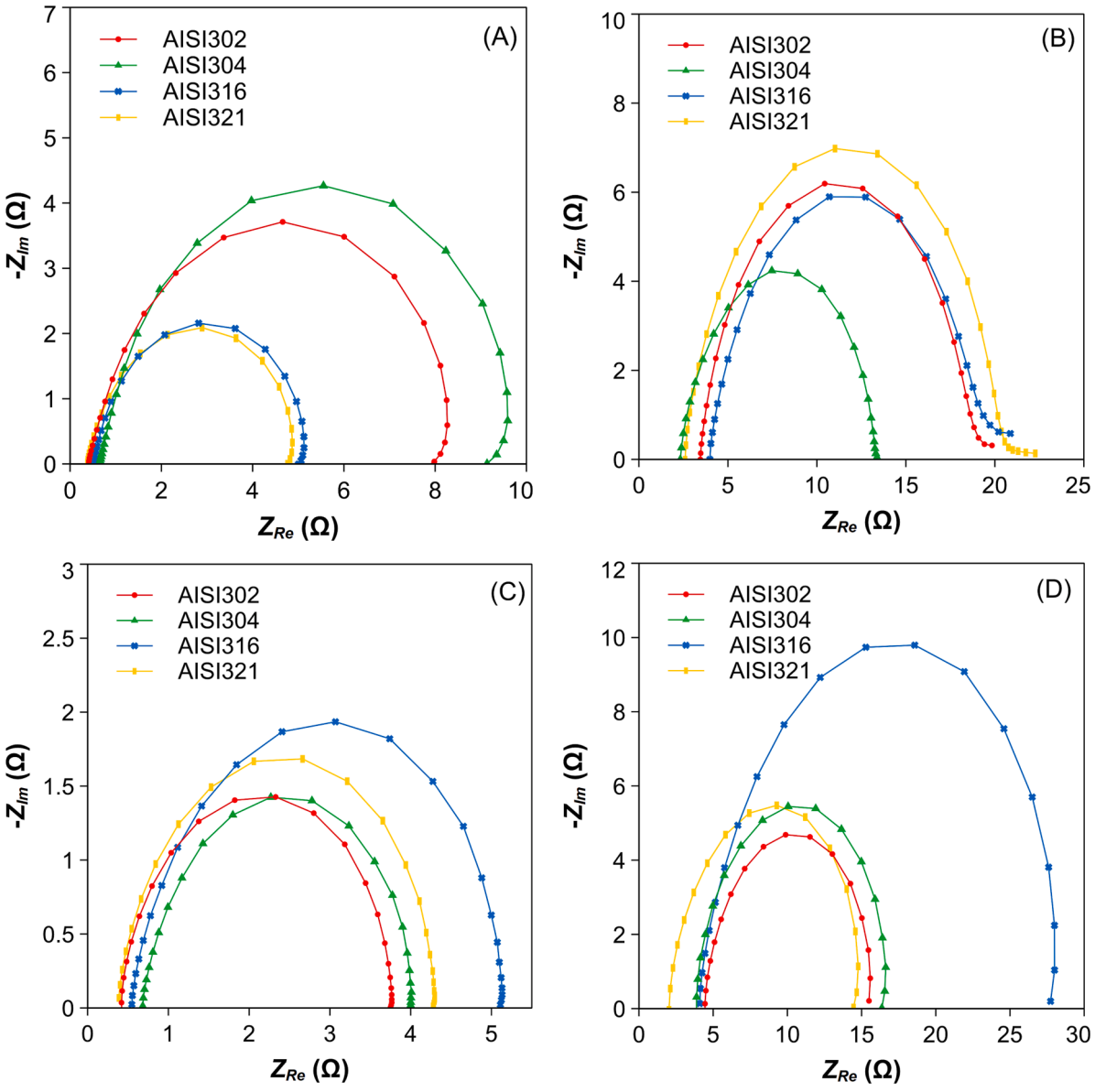

Fig. 8. Nyquist plots of AISI type steels in 1.0 M KOH (A, C) and 0.1 M KNO_3 (B, D) at OER (A, B) and HER (C, D) onset potentials.

Table 7
Equivalent circuit parameters, fitted with equivalent circuit $R_s + C_{dl}/R_{ct}$, of various SSs in alkaline and neutral electrolyte at OER and HER onset potentials, where R_s is the solution resistance, C_{dl} is the double layer capacitance and R_{ct} is the charge transfer resistance.

Reaction	EC component	Stainless steel type			
		AISI302	**AISI304**	**AISI316**	**AISI321**
Alkaline media					
OER	R_s (Ω)	0.5	0.9	0.5	0.4
	C_{dl} (mF)	1.3	1.1	1.5	1.6
	R_{ct} (Ω)	7.7	8.7	4.4	4.6
HER	R_s (Ω)	0.5	0.7	0.6	0.5
	C_{dl} (mF)	0.4	0.3	0.4	0.3
	R_{ct} (Ω)	3.2	3.1	4.2	3.6
Neutral media					
OER	R_s (Ω)	3.8	2.7	4.3	2.9
	C_{dl} (mF)	0.5	0.5	0.6	0.4
	R_{ct} (Ω)	13.0	10.7	13.8	16.5
HER	R_s (Ω)	4.7	3.8	4.4	2.4
	C_{dl} (mF)	0.2	0.1	0.2	0.1
	R_{ct} (Ω)	10.5	12.3	23.9	12.7

plots of SS samples recorded under alkaline (A, C) and neutral (B, D) conditions. The curves were fitted with equivalent circuit $R_s + C_{dl}/R_{ct}$ and the values of the circuit components R_s (solution resistance), C_{dl} (double layer capacitance), and R_{ct} (charge transfer resistance) were calculated (Table 7). During this experiment, it was noticed that hydrogen evolution in alkaline solution occurs with the lowest charge transfer resistance (3.1–4.2 Ω) if compared to other processes investigated. This result might be associated with a favorable metal role as the electron donor. Although OER is a more challenging reaction than HER even in an alkaline electrolyte, the R_{ct} values of AISI steels have reached a promising result that varies from 4.4 Ω (AISI316) to 8.7 Ω (AISI304). When discussing the charge transfer differences in HER and OER, the increase in R_{ct} might also be associated with an increase in double layer, as the formation of oxo species on the surface during the OER might block the charge transfer processes [43]. This assumption is also supported by the calculation of the C_{dl} values (Table 7) that increase up to 4 times from 0.35 ± 0.05 mF (HER) to 1.4 ± 0.3 mF (OER) when the reaction switches from reduction (HER) to oxidation (OER). Replacement of the alkaline solution with a neutral one appears to reduce the double layer, as its capacitance values regardless of the process (OER or HER) are much smaller and range from 0.15 mF (HER) to 0.5 mF (OER). As in the case of an alkaline electrolyte, reduction processes on steels in 0.1 M KNO_3 occur with the formation of a smaller double layer than oxidation. However, the charge-transfer resistance increases significantly when water molecules are adsorbed onto the surface instead of hydroxide ions. This regularity is particularly characteristic for the AISI316 type steel, which indicates the high values of R_{ct} for both OER (13.8 Ω) and HER (23.9 Ω). The higher resistance to transfer of electrons at the electrode/electrolyte interface during redox reactions could be responsible for the drop in the electrocatalytic activity of AISI316 in neutral medium (Fig. 6B). As the corrosion rate of this steel is one of the highest under neutral conditions (Table 6), it is likely that the formation of a passivation film in the presence of water molecules can hinder its catalytic application.

4. Conclusions

The detailed electrochemical investigation of four types of commercially available AISI stainless steel has revealed their efficiency in catalyzing both half reactions of water splitting – OER and HER. Although less harsh conditions with near neutral pH are desired for water splitting due to environmental and economic aspects, the alkaline electrolyte has shown its advantage since a current density of 10 mA cm^{-2} is reached at η≈0.38 V for OER and η≈0.43 V for HER. The differences in activity among AISI steels which arise mainly in alkaline solution might come from changes in electron density due to the hypo-hyper-d effect, especially when Mo or Ti is introduced into the alloy. Meanwhile, when it comes to the adsorption of water molecules instead of hydroxyl ions, these elements do not play such an important role and their efficiency becomes almost equal. Corrosion evaluation has shown that regardless of the pH value of the electrolyte, the tendency of AISI302 and AISI316 to oxidize is clearly visible. Corrosion rate calculations revealed that probably due to the formation of a passivating oxide film on the surface of the SS, the rate is relatively low and is approximately 2 and 0.5 μm per year under alkaline and neutral conditions, respectively.

Funding

This work was supported by the Research Council of Lithuania [grant number P-PD-22-129].

CRediT authorship contribution statement

Ieva Barauskienė: Conceptualization, Methodology, Software, Validation, Investigation, Resources, Data curation, Writing – original draft, Visualization. **Giedrius Laukaitis:** Methodology, Software, Validation, Formal analysis, Investigation, Data curation, Writing – review & editing. **Eugenijus Valatka:** Conceptualization, Writing – review & editing.

Declaration of Competing Interest

The authors declare that they have no known competing financial interests or personal relationships that could have appeared to influence the work reported in this paper.

Appendix A. Supplementary material

Supplementary data associated with this article can be found, in the online version, at https://doi.org/10.1016/j.jelechem.2023.117880.

References

[1] C. Santoro, A. Lavacchi, P. Mustarelli, V. Di Noto, L. Elbaz, D.R. Dekel, F. Jaouen, What is next in anion-exchange membrane water electrolyzers? bottlenecks, benefits, and future, ChemSusChem 15 (2022), https://doi.org/10.1002/cssc.202200027.
[2] IRENA, Hydrogen from renewable power: Technology outlook for the energy transition, (2018).
[3] C. Hu, L. Zhang, J. Gong, Recent progress made in the mechanism comprehension and design of electrocatalysts for alkaline water splitting, Energy Environ. Sci. 12 (2019) 2620–2645, https://doi.org/10.1039/c9ee01202h.
[4] H.A. Miller, K. Bouzek, J. Hnat, S. Loos, C.I. Bernäcker, T. Weißgärber, L. Röntzsch, J. Meier-Haack, Green hydrogen from anion exchange membrane water electrolysis: a review of recent developments in critical materials and operating conditions, Sustainable Energy Fuels 4 (2020) 2114–2133, https://doi.org/10.1039/C9SE01240K.
[5] R.R. Raja Sulaiman, W.Y. Wong, K.S. Loh, Recent developments on transition metal-based electrocatalysts for application in anion exchange membrane water electrolysis, Int. J. Energy Res. 46 (2022) 2241–2276, https://doi.org/10.1002/er.7380.
[6] I. Vincent, D. Bessarabov, Low cost hydrogen production by anion exchange membrane electrolysis: a review, Renew. Sustain. Energy Rev. 81 (2018) 1690–1704, https://doi.org/10.1016/j.rser.2017.05.258.
[7] S.M.A. Nayem, S. Islam, M.A. Aziz, A.J.S. Ahammad, Mechanistic insight into hydrothermally prepared molybdenum-based electrocatalyst for overall water splitting, Electrochim. Acta 445 (2023) 142050.
[8] G. Huang, M. Hu, X. Xu, A.A. Alothman, M.S.S. Mushab, S. Ma, P.K. Shen, J. Zhu, Y. Yamauchi, Optimizing heterointerface of Co2P-CoxOy nanoparticles within a porous carbon network for deciphering superior water splitting, Small Struct. 4 (2023), https://doi.org/10.1002/sstr.202200235.
[9] R.B. Ghising, U.N. Pan, D.R. Paudel, M.R. Kandel, N.H. Kim, J.H. Lee, A hybrid trimetallic-organic framework-derived N, C co-doped Ni-Fe-Mn-P ultrathin nanosheet electrocatalyst for proficient overall water-splitting, J. Mater. Chem. A Mater. 10 (2022) 16457–16467, https://doi.org/10.1039/d2ta02470e.
[10] X. Wang, G. Huang, Z. Pan, S. Kang, S. Ma, P.K. Shen, J. Zhu, One-pot synthesis of Mn2P-Mn2O3 heterogeneous nanoparticles in a P, N -doped three-dimensional porous carbon framework as a highly efficient bifunctional electrocatalyst for

overall water splitting, Chem. Eng. J. 428 (2022), 131190, https://doi.org/10.1016/j.cej.2021.131190.
[11] W. Wu, Y. Huang, X. Wang, P.K. Shen, J. Zhu, Composition-optimized manganese phosphide nanoparticles anchored on porous carbon network for efficiently electrocatalytic hydrogen evolution, Chem. Eng. J. 469 (2023), 143879, https://doi.org/10.1016/j.cej.2023.143879.
[12] S.G. Neophytides, K. Murase, S. Zafeiratos, G. Papakonstantinou, F.E. Paloukis, N. V. Krstajic, M.M. Jaksic, Composite hypo-hyper-d-intermetallic and interionic phases as supported interactive electrocatalysts, J. Phys. Chem. B 110 (7) (2006) 3030–3042.
[13] M.M. Jaksic, Hypo-hyper-d-electronic interactive nature of synergism in catalysis and electrocatalysis for hydrogen reactions, Electrochim. Acta 45 (2000) 4085–4099, https://doi.org/10.1016/S0013-4686(00)00525-9.
[14] S.G. Neophytides, S. Zafeiratos, G.D. Papakonstantinou, J. Jaksic, F.E. Paloukis, M. M. Jaksic, Extended Brewer hypo-hyper-d-interionic bonding theory – I. Theoretical considerations and examples for its experimental confirmation, Int. J. Hydrogen Energy 30 (2005) 131–147, https://doi.org/10.1016/j.ijhydene.2004.05.008.
[15] F. Yu, F. Li, L. Sun, Stainless steel as an efficient electrocatalyst for water oxidation in alkaline solution, Int. J. Hydrogen Energy 41 (2016) 5230–5233, https://doi.org/10.1016/j.ijhydene.2016.01.108.
[16] H. Schaefer, M. Chatenet, Steel: the resurrection of a forgotten water-splitting catalyst, ACS Energy Lett. 3 (2018) 574–591, https://doi.org/10.1021/acsenergylett.8b00024.
[17] M. Kim, Y.-T. Kim, J. Choi, Controlled contribution of Ni and Cr cations to stainless steel 304 electrode: effect of electrochemical oxidation on electrocatalytic properties, Electrochem. Commun. 117 (2020) 106770.
[18] H. Schaefer, K. Kuepper, M. Schmidt, K. Mueller-Buschbaum, J. Stangl, D. Daum, M. Steinhart, C. Schulz-Koelbel, W. Han, J. Wollschlaeger, U. Krupp, P. Hou, X. Liu, Steel-based electrocatalysts for efficient and durable oxygen evolution in acidic media, Catal. Sci. Technol. 8 (2018) 2104–2116, https://doi.org/10.1039/c7cy02194a.
[19] S. Anantharaj, M. Venkatesh, A.S. Salunke, T.V.S.V. Simha, V. Prabu, S. Kundu, High-performance oxygen evolution anode from stainless steel via controlled surface oxidation and Cr removal, ACS Sustain. Chem. Eng. 5 (2017) 10072–10083, https://doi.org/10.1021/acssuschemeng.7b02090.
[20] E. Gileadi, E. Kirowa-Eisner, Some observations concerning the Tafel equation and its relevance to charge transfer in corrosion, Corros. Sci. 47 (2005) 3068–3085, https://doi.org/10.1016/j.corsci.2005.05.044.
[21] D. Antipin, M. Risch, Calculation of the Tafel slope and reaction order of the oxygen evolution reaction between pH 12 and pH 14 for the adsorbate mechanism, Electrochem. Sci Adv. (2022).
[22] M. Kovendhan, H. Kang, S. Jeong, J.S. Youn, I. Oh, Y.K. Park, K.J. Jeon, Study of stainless steel electrodes after electrochemical analysis in sea water condition, Environ. Res. 173 (2019) 549–555, https://doi.org/10.1016/j.envres.2019.03.069.
[23] S. Ramya, T. Anita, H. Shaikh, R.K. Dayal, Laser Raman microscopic studies of passive films formed on type 316LN stainless steels during pitting in chloride solution, Corros. Sci. 52 (2010) 2114–2121, https://doi.org/10.1016/j.corsci.2010.02.028.
[24] L. Bellot-Gurlet, D. Neff, S. Réguer, J. Monnier, M. Saheb, P. Dillmann, Raman studies of corrosion layers formed on archaeological irons in various media, J. Nano Res. 8 (2009) 147–156, https://doi.org/10.4028/www.scientific.net/JNanoR.8.147.
[25] J.F.W. Bowles, Hydroxides, in: D. Alderton, S.A. Elias (Eds.), Encyclopedia of Geology (second Edition), Academic Press, Oxford, 2021, pp. 442–451, https://doi.org/10.1016/B978-0-08-102908-4.00162-4.
[26] X. Liu, J. Meng, J. Zhu, M. Huang, B.o. Wen, R. Guo, L. Mai, Comprehensive understandings into complete reconstruction of precatalysts: synthesis, applications, and characterizations, Adv. Mater. 33 (32) (2021), https://doi.org/10.1002/adma.202007344.
[27] A. Valdes, J. Brillet, M. Graetzel, H. Gudmundsdottir, H.A. Hansen, H. Jonsson, P. Kluepfel, G.-J. Kroes, F. Le Formal, I.C. Man, R.S. Martins, J.K. Norskov, J. Rossmeisl, K. Sivula, A. Vojvodic, M. Zach, Solar hydrogen production with semiconductor metal oxides: new directions in experiment and theory, PCCP 14 (2012) 49–70, https://doi.org/10.1039/c1cp23212f.
[28] Z. Chen, X. Liu, T. Shen, C. Wu, L. Zu, L. Zhang, Porous NiFe alloys synthesized via freeze casting as bifunctional electrocatalysts for oxygen and hydrogen evolution reaction, Int. J. Hydrogen Energy 46 (2021) 37736–37745, https://doi.org/10.1016/j.ijhydene.2021.09.059.
[29] B. Zhang, F. Yang, X. Liu, N.i. Wu, S. Che, Y. Li, Phosphorus doped nickel-molybdenum aerogel for efficient overall water splitting, Appl. Catal. B-Environ. 298 (2021) 120494.
[30] E. Jiang, J. Li, X. Li, A. Ali, G. Wang, S. Ma, P. Kang Shen, J. Zhu, MoP-Mo2C quantum dot heterostructures uniformly hosted on a heteroatom-doped 3D porous carbon sheet network as an efficient bifunctional electrocatalyst for overall water splitting, Chem. Eng. J. 431 (2022), 133719, https://doi.org/10.1016/j.cej.2021.133719.
[31] W. Hua, H.-H. Sun, F. Xu, J.-G. Wang, A review and perspective on molybdenum-based electrocatalysts for hydrogen evolution reaction, Rare Met. 39 (2020) 335–351, https://doi.org/10.1007/s12598-020-01384-7.
[32] J.M. Jaksic, N.M. Ristic, N.V. Krstajic, M.M. Jaksic, Electrocatalysis for hydrogen electrode reactions in the light of Fermi dynamics and structural bonding factors – I. Individual electrocatalytic properties of transition metals, Int. J. Hydrogen Energy. 23 (1998) 1121–1156, https://doi.org/10.1016/S0360-3199(98)00014-7.
[33] Y. Xu, C. Wang, Y. Huang, J. Fu, Recent advances in electrocatalysts for neutral and large-current-density water electrolysis, Nano Energy 80 (2021) 105545.
[34] M. Plevová, J. Hnát, K. Bouzek, Electrocatalysts for the oxygen evolution reaction in alkaline and neutral media. A comparative review, J. Power Sources 507 (2021) 230072.
[35] R. Guidelli, R.G. Compton, J.M. Feliu, E. Gileadi, J. Lipkowski, W. Schmickler, S. Trasatti, Defining the transfer coefficient in electrochemistry: An assessment (IUPAC Technical Report), Pure Appl.ed Chem. 86 (2014) 245–258, https://doi.org/10.1515/pac-2014-5026.
[36] S. Fletcher, Tafel slopes from first principles, J. Solid State Electrochem. 13 (2009) 537–549, https://doi.org/10.1007/s10008-008-0670-8.
[37] S. Zhang, X. Zhang, Y. Rui, R. Wang, X. Li, Recent advances in non-precious metal electrocatalysts for pH-universal hydrogen evolution reaction, Green Energy Environ. 6 (2021) 458–478, https://doi.org/10.1016/j.gee.2020.10.013.
[38] W. Sheng, M. Myint, J.G. Chen, Y. Yan, Correlating the hydrogen evolution reaction activity in alkaline electrolytes with the hydrogen binding energy on monometallic surfaces, Energy Environ. Sci. 6 (2013) 1509–1512, https://doi.org/10.1039/c3ee00045a.
[39] Q. Lu, G.S. Hutchings, W. Yu, Y. Zhou, R.V. Forest, R. Tao, J. Rosen, B. T. Yonemoto, Z. Cao, H. Zheng, J.Q. Xiao, F. Jiao, J.G. Chen, Highly porous non-precious bimetallic electrocatalysts for efficient hydrogen evolution, Nat. Commun. 6 (2015), https://doi.org/10.1038/ncomms7567.
[40] S. Wang, A. Lu, C.-J. Zhong, Hydrogen production from water electrolysis: role of catalysts, Nano Converg. 8 (2021), https://doi.org/10.1186/s40580-021-00254-x.
[41] G.H.A. Therese, P.V. Kamath, Electrochemical synthesis of metal oxides and hydroxides, Chem. Mater. 12 (2000) 1195–1204, https://doi.org/10.1021/cm990447a.
[42] T. Shinagawa, A.T. Garcia-Esparza, K. Takanabe, Insight on Tafel slopes from a microkinetic analysis of aqueous electrocatalysis for energy conversion, Sci. Rep. 5 (2015), https://doi.org/10.1038/srep13801.
[43] H. Liang, M. Xu, E. Asselin, Corrosion of monometallic iron- and nickel-based electrocatalysts for the alkaline oxygen evolution reaction: A review, J. Power Sources 510 (2021) 230387.
[44] M.E.G. Lyons, M.P. Brandon, Redox switching and oxygen evolution electrocatalysis in polymeric iron oxyhydroxide films, PCCP 11 (2009) 2203–2217, https://doi.org/10.1039/b815338h.
[45] S.L. Medway, C.A. Lucas, A. Kowal, R.J. Nichols, D. Johnson, In situ studies of the oxidation of nickel electrodes in alkaline solution, J. Electroanal. Chem. 587 (2006) 172–181, https://doi.org/10.1016/j.jelechem.2005.11.013.
[46] M.W. Louie, A.T. Bell, An investigation of thin-film Ni-Fe oxide catalysts for the electrochemical evolution of oxygen, J. Am. Chem. Soc. 135 (2013) 12329–12337, https://doi.org/10.1021/ja405351s.
[47] S. Anantharaj, H. Sugime, B. Chen, N. Akagi, S. Noda, Boosting the oxygen evolution activity of copper foam containing trace Ni by intentionally supplementing Fe and forming nanowires in anodization, Electrochim. Acta 364 (2020) 137170.
[48] X. Chen, X.G. Li, C.W. Du, Y.F. Cheng, Effect of cathodic protection on corrosion of pipeline steel under disbonded coating, Corros. Sci. 51 (2009) 2242–2245, https://doi.org/10.1016/j.corsci.2009.05.027.